Mediterranean wave climate variability and its links with NAO and Indian Monsoon

Article *in* Climate Dynamics · November 2005

DOI: 10.1007/s00382-005-0025-4

2 authors:

P. Lionello
Università del Salento
237 PUBLICATIONS **7,233** CITATIONS
SEE PROFILE

Antonella Sanna
Centro Euro-Mediterraneo sui Cambiamenti Climatici
24 PUBLICATIONS **1,169** CITATIONS
SEE PROFILE

Climate Dynamics (2005) 25: 611–623
DOI 10.1007/s00382-005-0025-4

P. Lionello · A. Sanna

Mediterranean wave climate variability and its links with NAO and Indian Monsoon

Received: 29 March 2004 / Accepted: 1 April 2005 / Published online: 11 August 2005

Abstract This study examines the variability of the monthly average significant wave height (SWH) field in the Mediterranean Sea, in the period 1958–2001. The analysed data are provided by simulations carried out using the WAM model (WAMDI group, 1988) forced by the wind fields of the ERA-40 (ECMWF Re-Analysis). Comparison with buoy observations, satellite data, and simulations forced by higher resolution wind fields shows that, though results underestimate the actual SWH, they provide a reliable representation of its real space and time variability. Principal component analysis (PCA) shows that the annual cycle is characterised by two main empirical orthogonal functions (EOF) patterns. Most inter-monthly variability is associated with the first EOF, whose positive/negative phase is due to the action of Mistral/Etesian wind regimes. The second EOF is related to the action of southerly winds (Libeccio and Sirocco). The annual cycle presents two main seasons, winter and summer characterised, the first, by the prevalence of eastwards and southeastwards propagating waves all over the basin, and the second, by high southwards propagating waves in the Aegean Sea and Levantin Basin. Spring and fall are transitional seasons, characterised by northwards and northeastwards propagating waves, associated to an intense meridional atmospheric circulation, and by attenuation and amplification, respectively, of the action of Mistral. These wave field variability patterns are associated with consistent sea level pressure (SLP) and surface wind field structures. The intensity of the SWH field shows large inter-annual and inter-decadal variability and a statistically significant decreasing trend of mean winter values. The winter average SWH is anti-correlated with the winter NAO (North Atlantic Oscillation) index, which shows a correspondingly increasing trend. During summer, a minor component of the wave field inter-annual variability (associated to the second EOF) presents a statistically significant correlation with the Indian Monsoon reflecting its influence on the meridional Mediterranean circulation. However, the SLP patterns associated with the SWH inter-annual variability reveal structures different from NAO and Monsoon circulation. In fact, wave field variability is conditioned by regional storminess in combination with the effect of fetch. The latter is likely to be the most important. Therefore, the inter-annual variability of the mean SWH is associated to SLP patterns, which present their most intense features above or close to Mediterranean region, where they are most effective for wave generation.

P. Lionello (✉)
Department of Materials Science, University of Lecce,
8, via Marzolo, 35100 Padova, Italy
E-mail: lionello@pd.infn.it
Tel.: +39-049-8277289
Fax: +39-049-8277282

A. Sanna
Department of Materials Science, University of Lecce,
Padova, Italy

1 Introduction

The Mediterranean region is characterised by intense synoptic scale activity, with features, which, though their amplitude is smaller than that of the Atlantic and Pacific regions, are evident in the global storm track structure. In fact, the Northern Hemisphere storm track presents a separate branch crossing the Mediterranean region, with areas of cyclogenesis in the western Mediterranean and of prevalent cyclolysis in the Central and Eastern Mediterranean. A fraction of cyclones moves also to Black Sea, Ukraine and Russia (Hoskins and Hodges 2002).

Cyclogenesis in the Mediterranean region is primarily caused by orographic effects (Buzzi and Tibaldi 1978). Nevertheless, the latent heat release, which is a usual mechanism of intensification of cyclogenesis, is impor-

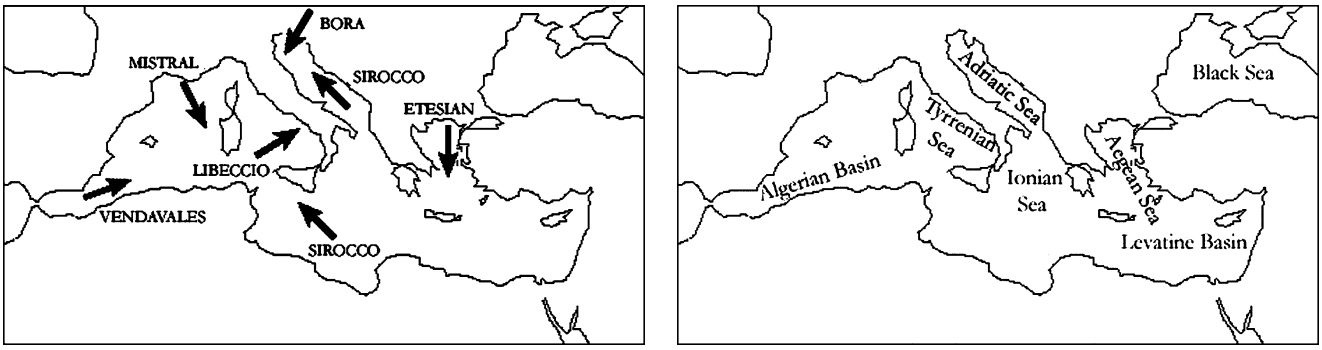

Fig. 1 *Left panel* shows main Mediterranean winds referred to in this paper; *right panel* shows the various basins considered. The area corresponds to the WAM model integration domain, except for the Black Sea, the Gulf of Biscay and the portion of the Atlantic west to the Strait of Gibraltar

tant too, especially in fall and winter, when the basin becomes a considerable heat reservoir (Trigo et al. 2002). Note that the Mediterranean Sea is characterised by high temperatures, so that in fall and winter there is a strong contrast with cold northerly air masses.

The Mediterranean is surrounded by a complex system of mountain chains, with crests ranging between 1,500 m and 4,800 m. This complex orography has the effect of distorting large synoptic structures and produces local winds of sustained speed (such as Bora, Mistral-Tramontana, Etesian winds, Fig. 1), which, over some areas of the region, burst almost all over the year. Wave fields dynamics is conditioned by such wind regimes. The practical aim of this study is to provide information on wave climate variability and trends for the last four decades of the twentieth century, such as it has already been provided for other basins (eg. Günter et al. 1998), which may be useful for long-term planning of coastal defences and development of economic marine activities.

The present study is based on three different sets of data: wave observations, which include buoy and satellite data, and the results of numerical model simulations. Continuous buoy observations are provided by the Italian National buoy network RON (Rete Ondametrica Nazionale, national wave network, Fig. 2). However, they allow a continuous reconstruction only in sparse locations and since 1989. About 9 years of satellite observations are provided by TOPEX-POSEIDON (wave data are available from 1993) with two passages per day above the Mediterranean Sea. Though greatly improving the spatial information with respect to buoy measurements, the satellite are quite far from providing a complete coverage of the Mediterranean Sea and the time series are too short for evaluating climate variability and trends. Consequently, at the moment, observations appear insufficient to identify decadal trends. Model simulations of waves in the Mediterranean Sea have been successfully carried out with spectral wave models (e.g. Cavaleri et al. 1991) and are presently included in the predictions carried out by several meteorological services, but even these datasets do not allow a reconstruction of decadal wave field variability. Such simulations present discontinuities (due to changes of the meteorological and wave models used to produce them) and/or systematic errors, mostly due to inadequate resolution of the wind fields used as forcing. In fact, generally, modelled wind field under-evaluation and missing features are source of similar shortcomings in the computed wave fields (Cavaleri and Bertotti 2004). These errors, which have been partially compensated by the progressive increase of model resolution, remain large in global reanalysis, which are relatively homogeneous datasets but, because of their rough resolution, are affected by systematic surface wind under-evaluation. The simulations used in this study to analyse the wave climate are based on the ERA-40 (ECMWF Re-Analysis, (Simmons et al. 2000)) The ERA-40 project has been recently carried through at ECWMF, providing a complete reconstruction of the atmospheric structure at T156 resolution (about 100 km), over the 44-year period from 1958 to 2001. It is therefore an homogeneous dataset, as model and data analysis methods are concerned[1], but its resolution is not sufficient for the Mediterranean basin. A possible solution is post-processing, consisting of re-scaling and re-shaping the wind fields, in order to compensate for these shortcomings (Lionello et al. 2003). Instead, this study avoids this procedure, computing dimensionless indexes and carrying out PCA and investigating whether this allows a reliable re-construction of the actual wave field variability.

Section 2 is devoted to climate model verification, in order to establish if the WAM model forced by ERA-40 re-analysis wind data can be used to produce a reliable wave climatology in the Mediterranean Sea. This is done by comparison between time series of buoy observations, satellite data and simulations driven by wind fields at higher resolution, covering the whole Mediterranean basin. In Sect. 3 a PCA is used to deduce the SWH annual cycle and the principal characteristic wave regimes. Section 4 looks into the presence of climatological trends in the 44-year ERA period and connections

[1]The meteorological observations used in the model cannot, however, be homogeneous during such a long period

Fig. 2 Buoys of the RON network around Italy. SWH observed data are available from 1989. Ancona and Cetraro stations are not used in this study, their data being available only from 1999

with large scale patterns, such as North Atlantic Oscillation (NAO) and Indian Monsoon. The outcomes of the study are summarised in Sect. 5.

2 Model climate verification

The present analysis is mainly based on the monthly average values of the WAM model simulation forced by the wind fields of ERA-40. The 10 m height wind fields (hereafter, U_{10}) are used as forcing term to drive a 44-year simulation (hereafter, SWHERA40), performed with WAM model (Wave Model cycle 4; WAMDI Group 1988), which is implemented over the whole Mediterranean Sea with a resolution of 25 km.

The first step is the assessment of the capability of SWHERA40 to represent the real wave fields. In fact, a widely discussed issue is the capability of model simulations to reproduce the mesoscale features of surface wind fields in the Mediterranean area and, consequently, to simulate adequately the wave fields. The comparison between model simulations at different resolution shows that average wave height increases with resolution (Cavaleri and Bertotti 2004). While on global scale there are indications that high resolution simulations (T799) are not far from the asymptotic level of satellite observations, independently from further resolution increase, this is not true on regional Mediterranean scale. The results suggest that a substantial further increase in resolution is needed. SWHERA40 simulation cannot therefore be expected to adequately reproduce the observed SWH values. However, this study does not aim to simulate in detail the real SWH values, but to identify the most important SWH monthly regimes and evaluate their inter-annual variability and trends in the last 44 years. To such purpose the SWH dimensionless index, denoted as $\mathrm{SWH}_i^{\mathrm{dataset}}$, for every month i of the simulation, has been defined from the monthly average SWH, computing its deviation from the mean annual cycle, and normalising it with the corresponding monthly standard deviation:

$$\mathrm{SWH}_i^{\mathrm{dataset}} = \frac{< \mathrm{swh}_i^{\mathrm{dataset}} > - \mathrm{swh}_{\mathrm{month}(i)}^{\mathrm{dataset}}}{\mathrm{STDEV}_{\mathrm{month}(i)}^{\mathrm{dataset}}}. \quad (1)$$

Here, $< \mathrm{swh}_i^{\mathrm{dataset}} >$ is the average monthly SWH value, $\mathrm{swh}_{\mathrm{month}(i)}^{\mathrm{dataset}}$ the value of the corresponding month in the mean annual cycle, and $\mathrm{STDEV}_{\mathrm{month}(i)}^{\mathrm{dataset}}$ its standard deviation. This SWH index is meant to retain the information on inter-annual variability, regardless of the actual magnitude of the signal, which is generally different in the observations and the model simulations. The set of data used for the computation of the index (denoted as dataset) in Eq. 1 is different if the whole wave field, satellite or buoy data are considered.

Figure 3, top panel, refers to the data at the RON buoys from 1992 to 2000. In this case the dataset consists of the buoy observations, SWHERA40 data of the SWH value at the sea point of the WAM model grid nearest to the buoy location. Figure 3, middle panel, shows the similar comparison but considering satellite data and co-located model points along the satellite

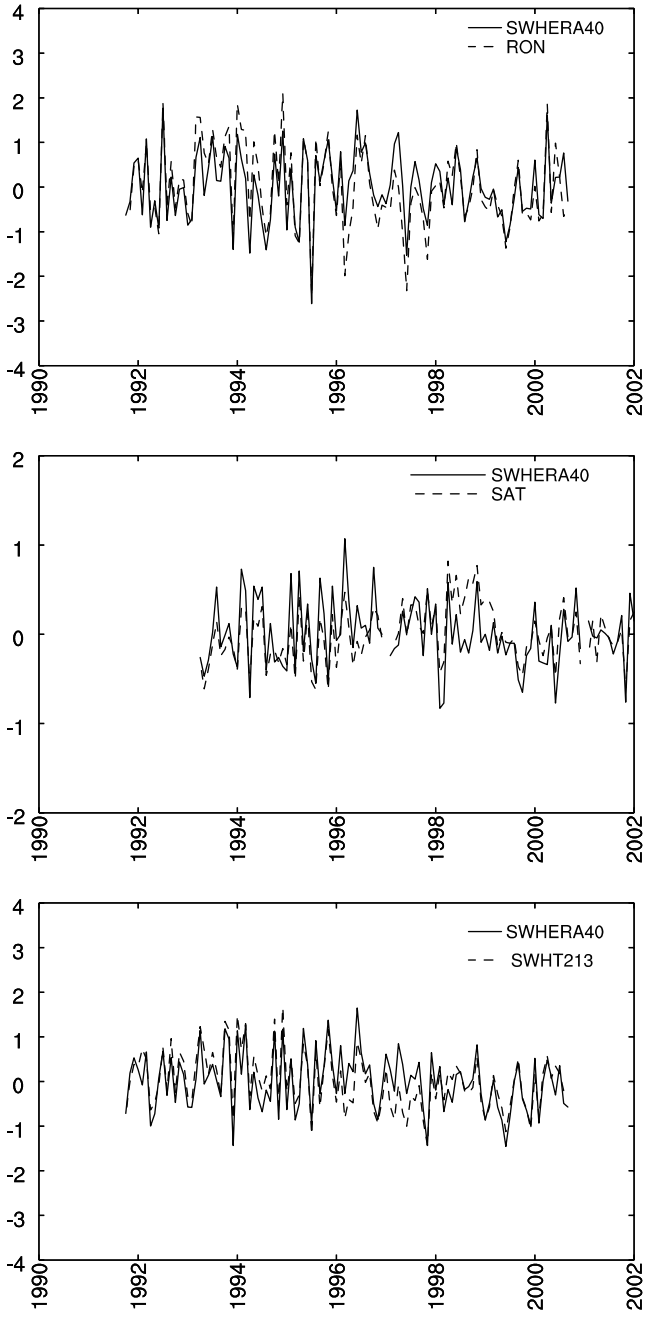

Fig. 3 Time series of the SWH index. *Top panel*, index based on values at the RON buoys: SWHERA40 (*continuous line*) and RON buoys(*dashed line*). *Middle panel*, index based on values along the satellite track: SWHERA40 (*continuous line*) and satellite SWH (*dashed line*). *Bottom panel*, index based on the whole integration domain: SWHERA40 (*continuous line*) and SWHT213 (*dashed line*)

track. The high correlation (Table 1) between model SWH and both satellite and buoy observations shows that the model reproduces realistically the observed inter-annual variability of monthly SWH values. Besides SWHERA40, another simulation (hereafter, SWHT213) has been carried out. SWHT213 has been performed at the same resolution of the SWHERA40, but driven by winds at a higher resolution (about 50 km) provided by T213 ECMWF model (Simmons 1991). SWHT213 covers only the last 10 years of twentieth century, while SWHERA40, covering a period of 44 years (1958–2001), is a more suitable tool for a climate analysis.

If the index is computed considering all points in the domain of the SWHERA40 and SWHT213 simulations (Fig. 3, bottom panel, Table 1), the results show that they contain a similar signal, regardless of their different resolution. The same is true as far as variability spatial structures are concerned. The PCA carried out both for SWHERA40 and SWHT213 result in similar EOFs (Fig. 6, first and second row, respectively). The comparison between the SWHERA40 and SWHT213 EOFs shows also that wind field resolution has no relevant effect on the mean wave propagation direction for this analysis.

Validation of SWHERA40 wave propagation directions can be based on buoys observations only, which could be strongly affected by the shape of the coastline. Figure 4 shows the cumulative distribution of the wave monthly mean propagation direction between SWHERA40 and RON buoys. Though there is a non-negligible (about 10%) probability of relevant discrepancies (larger than 90°), the error is lower than 30°, which is the angular resolution used for the WAM model spectrum, 60% of times.

These results support the claim that the SWHERA40 simulation is a suitable tool to describe climatological trends over Mediterranean Sea. From now the SWHERA40 SWH will be referred to simply as SWH.

Table 1 Correlation coefficients and 95% confidence intervals between SWHERA40 and SWHT213 (top row, computed considering the whole domains), RON buoys (middle row), TOPEX-POSEIDON data (bottom row, computed considering only co-located model and satellite data)

SWHERA40 correlation	
SWHT213	0.77 < 0.84 < 0.89
RON Buoys	0.84 < 0.89 < 0.92
TOPEX-POSEIDON	0.64 < 0.72 < 0.79

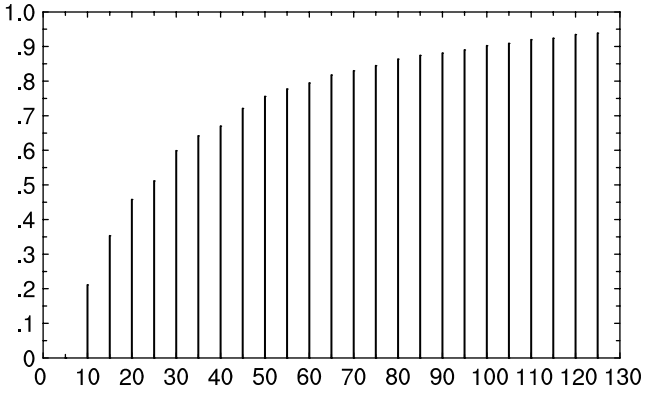

Fig. 4 Cumulative distribution (*Y*-axis) of monthly mean direction differences (*X*-axis, in degrees) between SWHERA40 and RON buoys

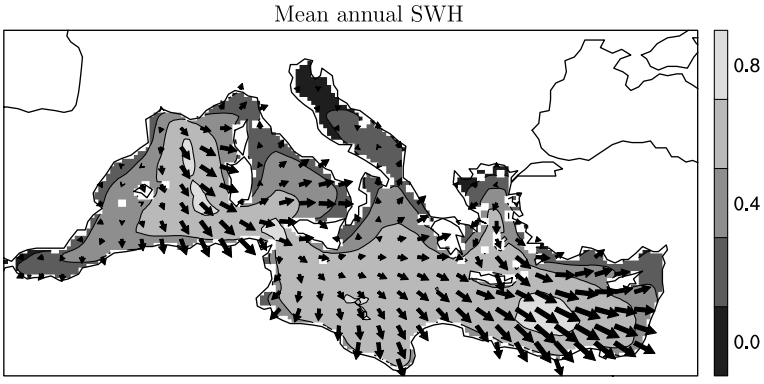

Fig. 5 Mean annual SWH field. The *arrows*, drawn every 1.25°, denote the mean wave propation direction. Contours level interval 0.2 m, from 0.0 m to 1.0 m

3 Characteristics of the annual cycle

The average SWH field (Fig. 5) shows the prevailing effect of northwesterly winds on annual scale over most of the basin. The variability superimposed to this average pattern has been evaluated by PCA of the monthly average SWH. The data used consist of a vector whose magnitude is the SWH and direction the mean wave propagation direction. The PCA has been jointly applied to its meridional and zonal component. This statistical technique (Von Storch and Zwiers 1999) is widely used in climatological analyses, allowing to discriminate, inside the enormous amount of data characterising the real system, between the meaningful component and the "noise", which can be considered irrelevant in the process description and understanding. PCA is based on an eigenproblem, which naturally arises maximising the quadratic propriety of the variance. The new basis resulting from this procedure consists of the empirical orthogonal functions (EOFs), orthogonal spatial patterns which identify the preferred modes of variability of the considered system. The time coefficients obtained projecting the fields onto the EOFs are called principal components (hereafter, PC), are uncorrelated and represent the variability of the field. When this technique is applied to the SWH monthly average fields, results show that most variability is described by the first two EOFs, accounting for 51% and 22% of the total variance, respectively (Fig. 6, first row, Table 2). First EOF reveals the presence of waves travelling southeastwards in the western part of the basin, eastwards in the central part and turning northeastwards in the Levantine Basin.

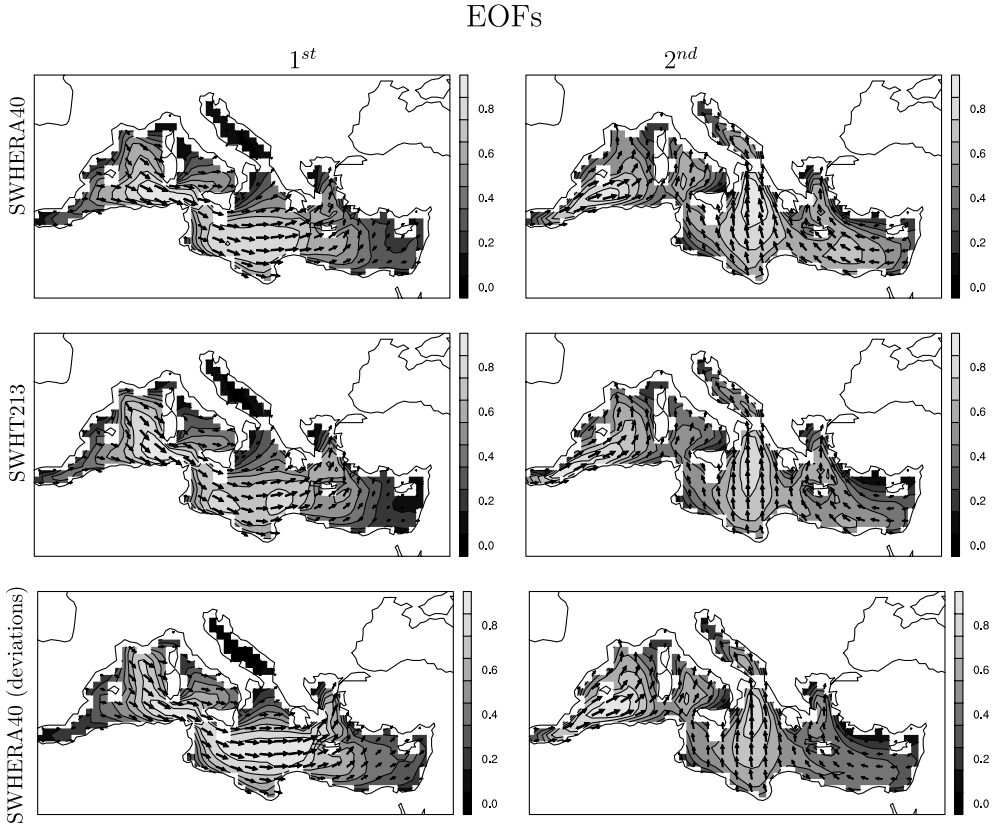

Fig. 6 First and second EOFs (*left and right panel*, respectively). First row: SWHERA40 monthly average fields; second row: SWHT213 monthly average fields; third row: SWHERA40, monthly average deviations from the annual cycle. Contours level interval 0.1, from 0.0 m to 1.0 m. All patterns are normalised with their maximum value. The *arrows*, drawn every 1.5°, are associated to the mean wave propagation direction

Table 2 Percentage of variance explained by the first five EOFs of SWHERA40

Percentage variance EOFS	
EOF 1	50.65%
EOF 2	21.82%
EOF 3	7.10%
EOF 4	5.48%
EOF 5	3.38%

The second EOF is characterised by waves propagating northwards in the Ionian Sea, which become rather northeastward in the west and northwestward in the Levantine Basin.

The interpretation of the two dominant EOFs is based on the positive/negative composites of SWH, U_{10}, SLP (these last two fields extracted from ERA-40 dataset), obtained considering the average fields of the respective variables at times when the corresponding PC of the SWH field is in the uppermost/lowermost 10%

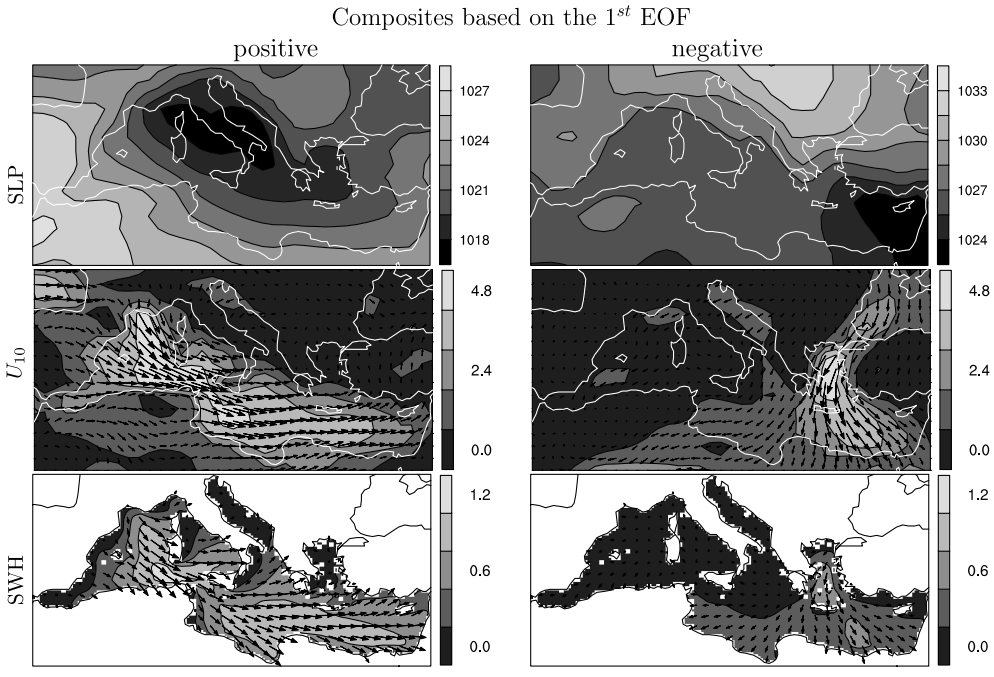

Fig. 7 Composites based on uppermost (*left column*) and lowermost (*right column*) 10% values of the SWH first PC: SLP (*top row*, contour level interval of 1 hPa, ranging according to the respective level bars), U_{10} (*middle row*, contour level interval of 1.2 m/s, from 0.0 m/s to 6.0 m/s), SWH (*bottom row*, contour level interval of 0.3 m, from 0.0 m to 1.5 m; the *direction of the arrows*, is associated to the mean direction of wave propagation. For both wind and waves, arrows are drawn every 1.25°

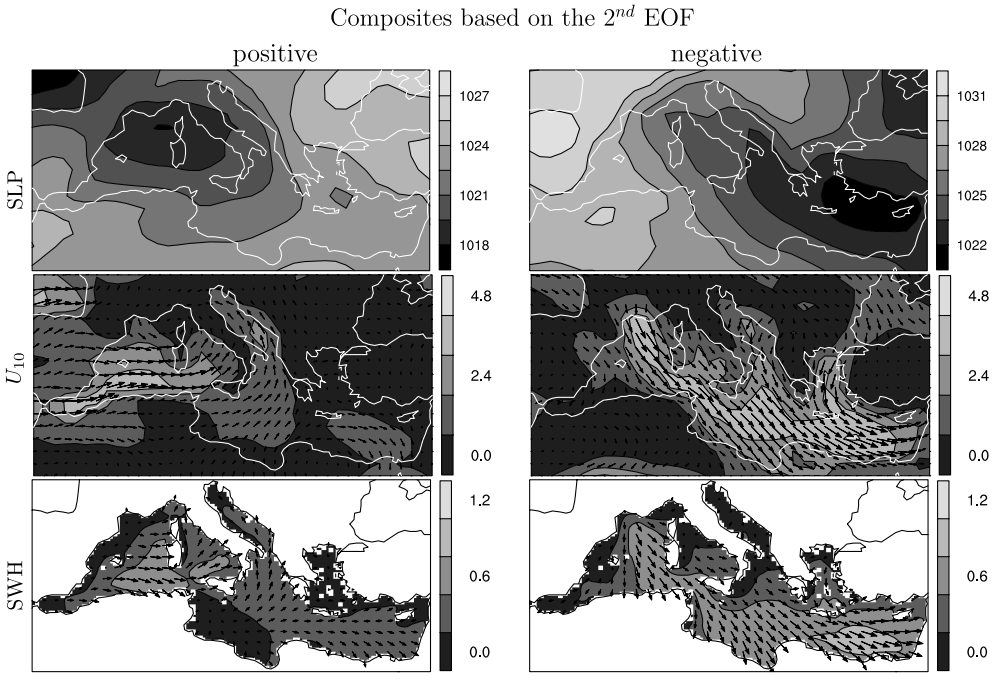

Fig. 8 Same as Fig. 7, but referring to the second EOF

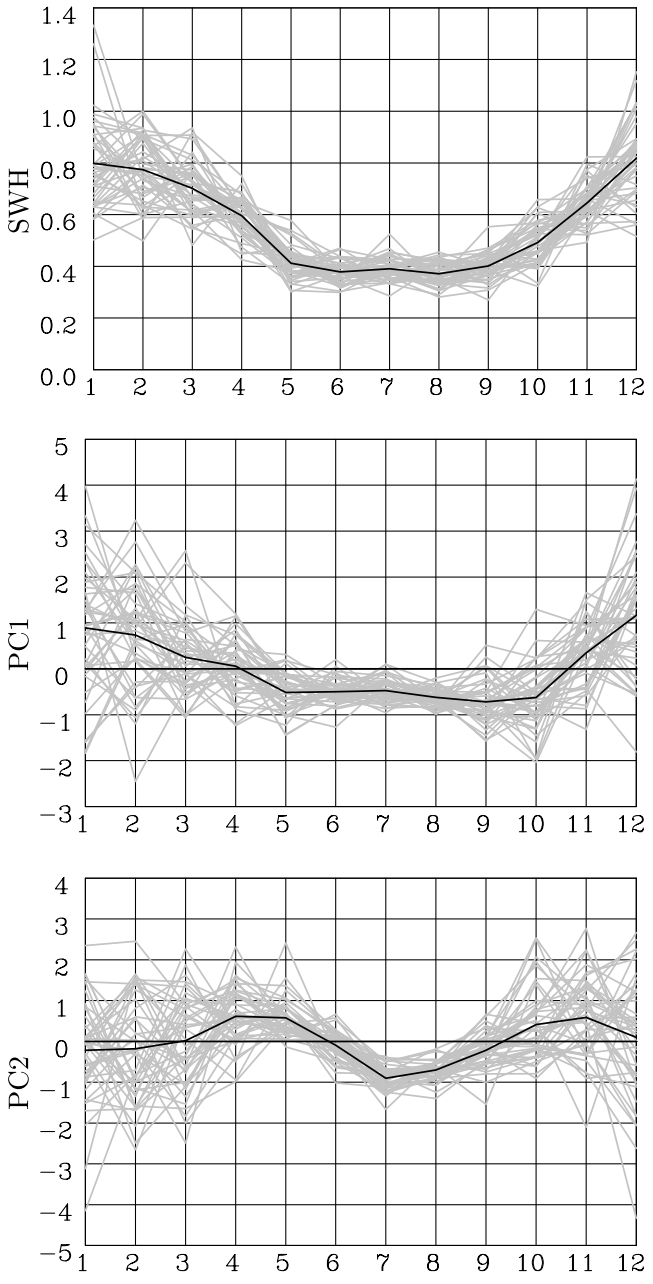

Fig. 9 Average monthly SWH (*top panel*; values in meters); first and second PCs (*middle and bottom panel*, respectively) normalised with the square root of the respective eigenvalue. In all panels, the *grey lines* represent individual years, the *black line* the average annual cycle. The x-axis reports the calendar months

range. The positive phase of the first EOF represents a strong Mistral circulation (Fig. 7, middle-left), associated with prevalent northwesterly winds and a low pressure system (Fig. 7, top-left panel) over the Italian peninsula. The corresponding SWH composite (Fig. 7, bottom-left panel) is dominated by strong waves in southwestern part of the Mediterranean, just offshore the Tunisian coast and in the Levantine Basin. The negative phase represents the effect of southward Etesian winds (Fig. 7, middle-right panel), associated with a pressure gradient constrained between a high pressure above continental Europe and a low pressure above Middle East (Fig. 7, top-right panel). This meteorological situation produces a wave field (Fig. 7, bottom-right panel), with peaks in the Aegean Sea and in the Levantine Basin. From now on, we will refer to this meteorological situation, associated to the first SWH EOF, as Mistral-Etesian-pattern: it is characterised by the transition from Etesian winds regime (negative phase) to Mistral regime (positive phase). During the positive phase of the second EOF, instead, the SLP minimum is located over the Gulf of Genoa (Fig. 8, top-left panel) and produces Sirocco, over Ionian and Adriatic Sea, strong Libeccio, over Tyrrenian, and Vendavales, over the Algerian Basin (Fig. 8, middle-left panel). The corresponding wave field is directed eastwards in the western basin, with the highest SWH peaks offshore of the Tunisian coast and in the Tyrrenian Sea, and northwestwards in the Adriatic Sea (Fig. 8, bottom-left panel). During its negative phase, a low pressure system is located on the Levantine basin (Fig. 8, top-right panel) and produces a southeastward circulation over most of the Mediterranean, resulting from the simultaneous presence of Etesian winds, in the eastern part, and Mistral, in the western part (Fig. 8, middle-right panel). As far as waves are concerned, the computed pattern (Fig. 8, bottom-right panel) presents a prevailing southeastwards system and the highest SWH level in the Levantine Basin. In the following, we will refer to this meteorological situation as to Libeccio-Sirocco-pattern.

The first two EOF patterns, described previously, present a clear annual cycle (Fig. 9). The first component splits the year into a period (November to April), characterised by waves produced by the Mistral wind, and another one, with a weaker signal, corresponding to those produced by Etesian winds. As this component represents a large fraction of the total variability, the annual cycle of the average SWH has a similar behaviour (Fig. 9). The computed correlation between the two series is in fact very high (correlation coefficient and 95% confidence interval: $-0.87 < -0.77 < -0.61$). The second component divides the year in four parts: the positive phase (Libeccio and Sirocco) characterises the periods Apr-May and Oct-Nov, while the negative one characterises the periods Feb-Mar and Jun-Aug. The average behaviour of the two components suggests to consider four seasons: winter (Dec-Jan-Feb-Mar) with waves generated by the Mistral wind, summer (Jun-Jul-Aug-Sep) with neither Mistral nor Libeccio, but waves generated by Etesian winds, spring (Apr-May) and fall (Oct-Nov), in the middle of which the Mistral-Etesian-pattern is switched off and on, respectively, and during which waves are mostly generated by the Libeccio and Sirocco winds. The second and third rows in Fig. 10 show the average SWH field for months representative of the average conditions of these four seasons: December (positive phase of the Mistral-Etesian-pattern, second row, left panel), May (Libeccio-Sirocco-pattern, third row, left panel), July (negative phase of the Mistral-Etesian-pattern, second row, right

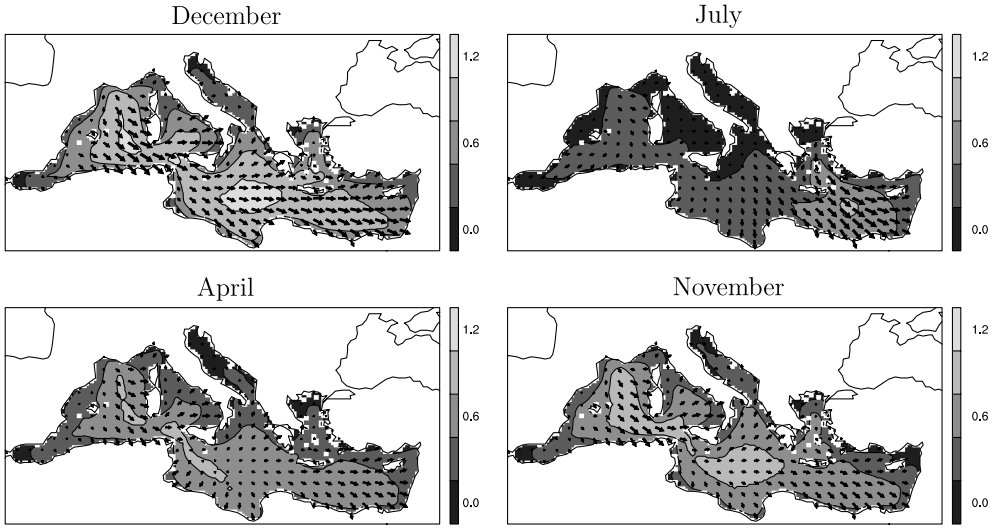

Fig. 10 Selected average monthly SWH field, computed over the whole 44-year SWHERA40 period. *Top panel*: December (*left*), representative of winter; July (*right*), representative of summer; *bottom panel*: April (*left*), representative of spring; November (*right*), representative of fall. Contours level interval 0.3 m, from 0.0 m to 1.5 m. *Arrows* show the mean wave propagation direction and contour levels the mean SWH value. *Short arrows* may indicate a region of high variability of wave direction

Table 3 Results of linear regression: second column shows slope and associated standard error; third column shows the confidence level calculated from an *F* test (Von Storch et al. 1999)

	Slope	C. level
Year		
SWH	-0.08 ± 0.03 cm year^{-1}	99%
PC1	-0.005 ± 0.003 year^{-1}	88%
PC2	-0.008 ± 0.003 year^{-1}	99.6%
Winter		
SWH	-0.24 ± 0.08 cm year^{-1}	94%
PC1	-0.016 ± 0.008 year^{-1}	93%
PC2	-0.008 ± 0.004 year^{-1}	95%
NAO	0.04 ± 0.01 year^{-1}	99.9%
Spring		
SWH	0.03 ± 0.06 cm year^{-1}	41%
PC1	0.001 ± 0.004 year^{-1}	18%
PC2	0.0008 ± 0.0022 year^{-1}	30%
Summer		
SWH	-0.04 ± 0.03 cm year^{-1}	83%
PC1	0.001 ± 0.001 year^{-1}	67%
PC2	0.0006 ± 0.0009 year^{-1}	48%
Fall		
SWH	0.07 ± 0.06 cm year^{-1}	76%
PC1	-0.002 ± 0.006 year^{-1}	23%
PC2	-0.006 ± 0.004 year^{-1}	89%

Internal table subheads refer to different periods: year, winter, spring, summer, fall and these consist of three rows showing results for: SWHERA40 SWH field averaged over the considered period (first row), first PC (second row) and second PC (third row) based on deviations from mean annual cycle. The winter table subhead presents a supplementary last row with the winter NAO index

panel), November (Libeccio-Sirocco-pattern, third row, right panel).

4 Inter-annual variability, trends, and links with NAO and Indian Monsoon

In order to investigate monthly inter-annual variability and trends in the wave climate, a PCA is carried out, on fields representing monthly average deviations from the annual cycle. The resulting EOFs are very similar to those obtained in the previous analysis (Fig. 6, compare first and third row). The recomputed first EOF differs from the previous for an intensification of Mistral effect and for a higher amplitude in the central region of the basin. The second presents a reduced variability in Levantine Basin. The strong similarity implies that inter-annual variability consists of changes of intensity or temporal shift of the same patterns characterising the annual cycle.

The 44-year time series of the average annual SWH exhibits a statistically significant trend (Table 3), corresponding to −0.08 cm/year reduction. Different seasons show different behaviour. Reduction is significant only in the winter season (−0.2 cm/year, Fig. 11), while the other seasons do not show statistically significant trends (Table 3). The same analysis performed on the PCs (Fig. 11, Table 3) shows that the SWH reduction of winter is associated with a decrease of both the first and the second PCs, but more relevant for the first. This means that reduction is mainly due to a weakening of the action of Mistral-Etesian-pattern on waves during winter.

The decreasing trend of winter SWH and first PC corresponds to the increase of the NAO[2] (Hurrel 1995)(Fig. 11, top-right). NAO index and SWH are, in fact, significantly correlated (Fig. 12, top panel, Table 4 left). Moreover, the NAO index shows a statistically significant correlation with both the first and the second PCs (Fig. 12, bottom panel, Table 4). The correlation is significantly larger for average SWH and first PC when the analysis is repeated filtering the data with a 5-year low-pass filter (Fig. 13, Table 4 right). The correlation is explained by the link between NAO and storminess in the Mediterranean region, as for large values of the

[2]The NAO index here used is obtained from PCA of 1,000 gph ERA-40 geopotential field; the correlation with the index computed in Jones et al. (1997) is 0.83.

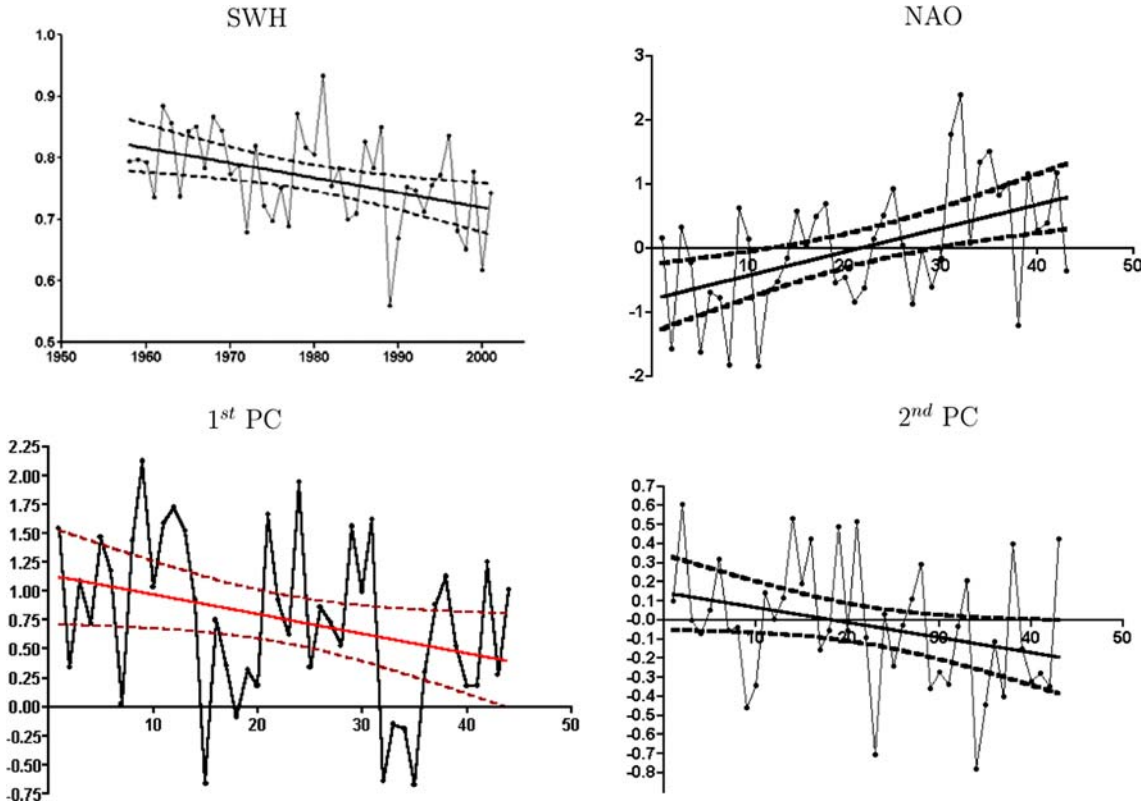

Fig. 11 Time series, linear regression (*strait line*) and 95% confidence interval (*dashed line*). *Top-left panel*: average winter SWH (values in meters). *Top-right panel*: winter mean NAO index. *Bottom-left panel*: first PC of SWH deviations from annual cycle, averaged over winter months (normalised with the square root of the corresponding eigenvalue). *Bottom-right panel*: as the bottom-left panel, but with reference to the second PC

NAO index the North Atlantic storm track deviates towards central and southern Europe, favouring high wind and waves conditions in the Mediterranean Sea.

In spite of the significant correlation between monthly average SWH and NAO index, the link between Mediterranean wave variability patterns and NAO is not so strong. As it was done in Sect. 3, SLP composites are here used to identify the meteorological patterns responsible for the variability of the mean seasonal wave fields. The SLP composites, based on winter months of the average SWH (Fig. 14, top-left panel), the first and the second PCs (Fig. 14, top-right and bottom-right panels, respectively, hereafter, winter-1 pattern and winter-2 pattern), show patterns different from NAO (Fig. 14, bottom-left panel). Here composites are obtained subtracting the average of the set of fields when the reference variable was in the 10% lowermost range to that when it was in the 10% uppermost range (i.e. subtracting the negative from the positive composite with reference to the definition in Sect. 3) . The winter-1 pattern and average SWH present a tripole with a principal minimum located over central Europe, a minor one in the Atlantic and a large maximum over north Atlantic, extending to Russia. On the Mediterranean region, it determines a strong atmospheric circulation, following the shape of the basin, with a prevailing southeastward direction in the western basin (absent in the NAO composite) and northeastward in the eastern one. The winter-2 pattern is dominated by the presence of a strong minimum over Gulf of Biscay determining a strong northward atmospheric circulation in the central Mediterranean Sea. The winter-1 and winter-2 patterns are the large scale SLP structures associated to the inter-annual variability of the seasonal regimes and can be partially associated to the Mistral-Etesian and Libeccio/Sirocco patterns, respectively, described in the previous Sect.3, as they produce similar wave variability in the Mediterranean Sea. Instead, NAO (Fig. 14, bottom-left panel), with the typical dipole located above the Atlantic and the corresponding zonal flow toward Europe, presents a weak circulation above the Mediterranean Sea, which cannot be associated with the intense components of the winter-1 and winter-2 patterns. The dependence of the wave regimes on the regional structures of the wind fields and on the land-sea distribution introduces necessarily a dependence on SLP regional features that are not associated with NAO. In other words, because of fetch effects, i.e. the modulation of the action of the wind by the land-sea distribution, the connection with NAO is distributed between two patterns, which are those favourable to the combination of long fetch and strong wind. If, as a countercheck, the NAO index is used for computing the composite of monthly average SWH deviations from annual cycle, the resulting pattern

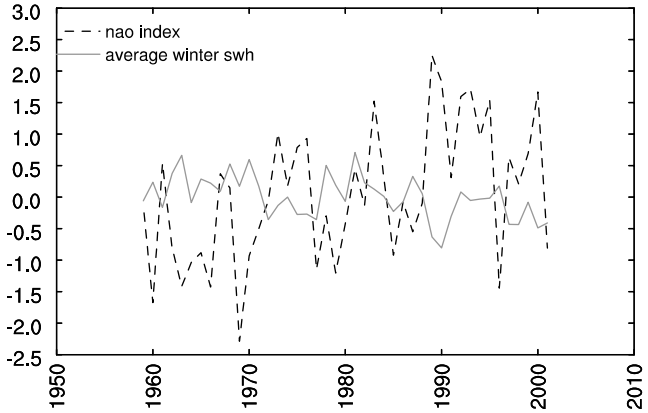

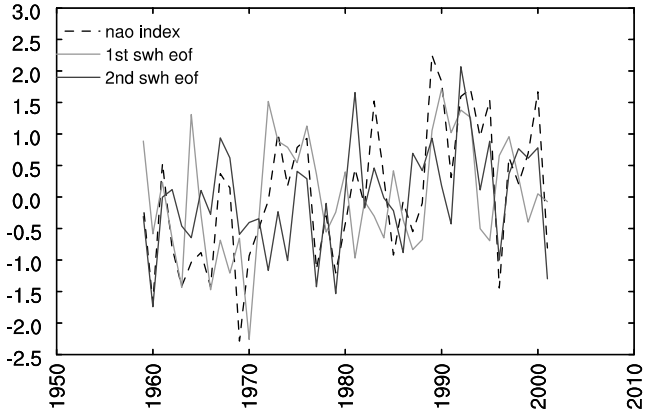

Fig. 12 Time series of winter NAO index and SWH plotted over the 44-year period. *Top panel* shows winter NAO index (*dashed black line*) and average winter SWH index (*light grey continuous line*). *Bottom panel* shows winter NAO index (*dashed black line*), winter average values of first PC (*light grey continuous line*) and second PC (*dark gray continuous line*)

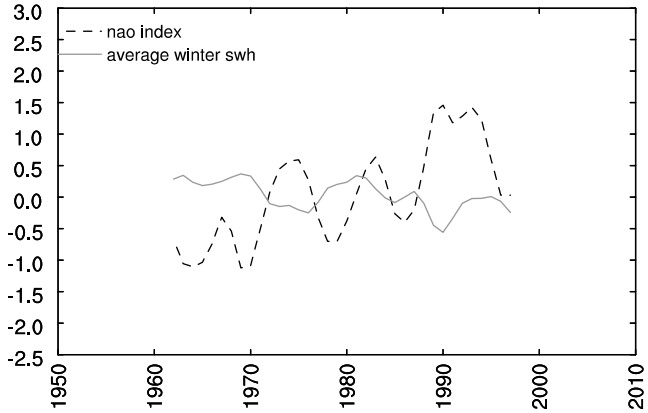

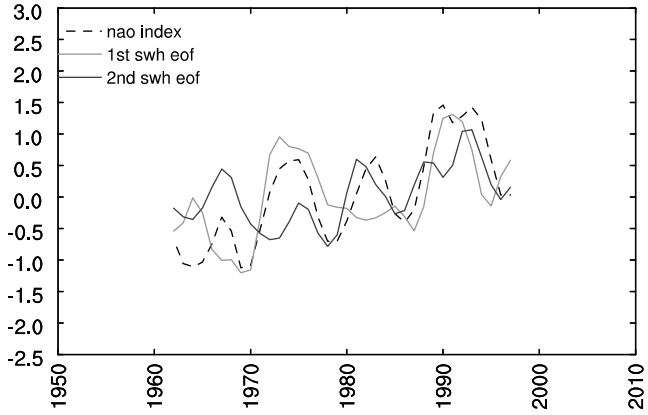

Fig. 13 Same as previous Fig. 12 but a 5-year low-pass filter is applied to the original time series. The period 1962–1998 is plotted

(Fig. 15) presents mostly features that are common with the second EOF, with which the NAO index is significantly correlated at the inter-annual time scale. More precisely, the northeastward wave propagation in the Algerian and Tyrrenian Sea, northward in the Ionian and northwestward along the Adriatic are also present in the second EOF.

During summer, a marginal relevance on the wave field variability is played by the Indian Monsoon (Kripalani and Kulkarni 2001) , which shows a statistically significant correlation with both average SWH and the second PCs (Table 5, Fig. 16). Applying to these time series a 5-year low-pass filter, both the correlation between average SWH and Monsoon index, and that between the second PC and the Monsoon index loose the statistical significance existing for inter-annual values (Table 5, right table, Fig. 17). However, though the SLP composite based on the second EOF (hereafter, summer-2 pattern, Fig. 18, bottom-right panel) presents some similarities on regional scale with that based on the Monsoon Index (see the pressure minimum over Spain, Fig. 18, bottom-left panel), this is not the case on large scale, where the characteristic pressure minimum over the Arabic Sea of the Monsoon composite is not present in the summer-2 pattern.

Table 4 Correlation coefficients and 95% confidence intervals

Correlation NAO-SWH		Correlation filtered NAO-SWH	
Average	$-0.67 < -0.47 < -0.19$	Average	$-0.94 < -0.73 < -0.13$
PC1	$-0.64 < -0.42 < -0.14$	PC1	$-0.94 < -0.73 < -0.12$
PC2	$0.47 < 0.67 < 0.81$	PC2	$-0.06 < 0.62 < 0.91$

Left table shows correlation coefficients computed for winter yearly values. First row exhibits correlation between NAO index and SWH index ; second and third row show correlation between NAO and first and second (respectively) PC of SWH values from which the annual cycle is subtracted. Right table shows results obtained after applying to data a 5-year low-pass filter; the coefficients are displayed following the same order of the left table

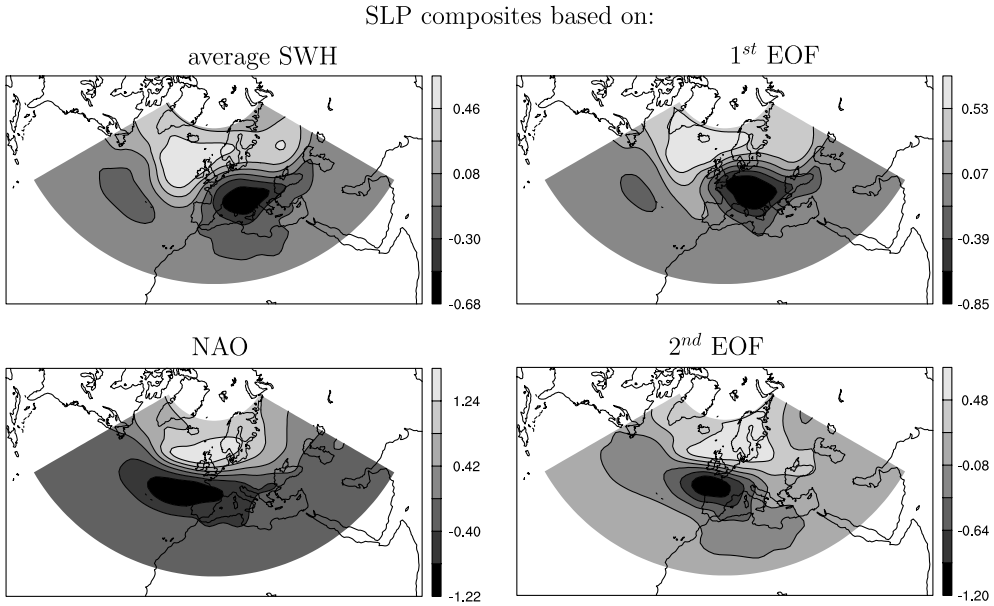

Fig. 14 Winter SLP composites based on monthly average SWH deviation from annual cycle (*top-left panel*); NAO index (*bottom-left panel*); first SWH EOF and second SWH EOF (*top-right and bottom-right panel*, respectively) computed on the base of deviations of monthly fields from mean annual cycle. Contour levels according to the level bars; values in hPa. These composites are obtained subtracting the average of the set of fields when the reference variable was in the 10% lowermost range to that when it was in the 10% uppermost range. Contours levels according to the level bars; values in hPa

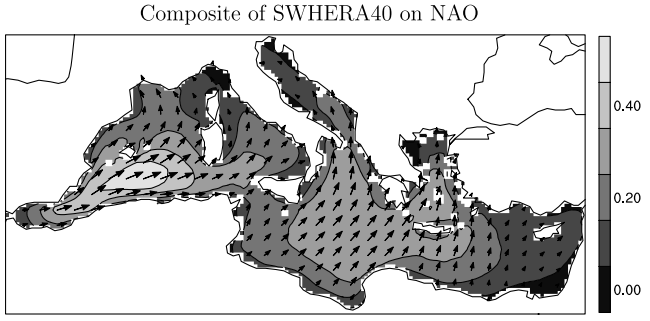

Fig. 15 Composite of monthly averaged SWH, obtained subtracting the fields corresponding to the 10% lowermost negative values of NAO index from those corresponding to the 10% uppermost positive values. Contours level interval 0.1, from 0.0 m to 0.6 m. The *direction of the arrows* represents the wave mean propagation direction

Table 5 Same as Table 4, but referring to the Indian Monsoon index and to summer

Correlation Monsoon-SWH		Correlation filtered Monsoon-SWH	
Average	$0.04 < 0.34 < 0.58$	Average	$-0.33 < 0.50 < 0.89$
PC1	$-0.15 < 0.16 < 0.45$	PC1	$-0.73 < -0.05 < 0.68$
PC2	$0.11 < 0.40 < 0.63$	PC2	$-0.33 < -0.09 < 0.65$

In conclusion, the SLP patterns associated to the main wave variability patterns present single intense centres very close to the Mediterranean Sea. The winter-1 pattern presents a large minimum over central Europe which moves eastward to the Aegean Sea in the summer-1 pattern. The winter-2 pattern, associated to the second SWH EOF, presents a minimum over East Atlantic

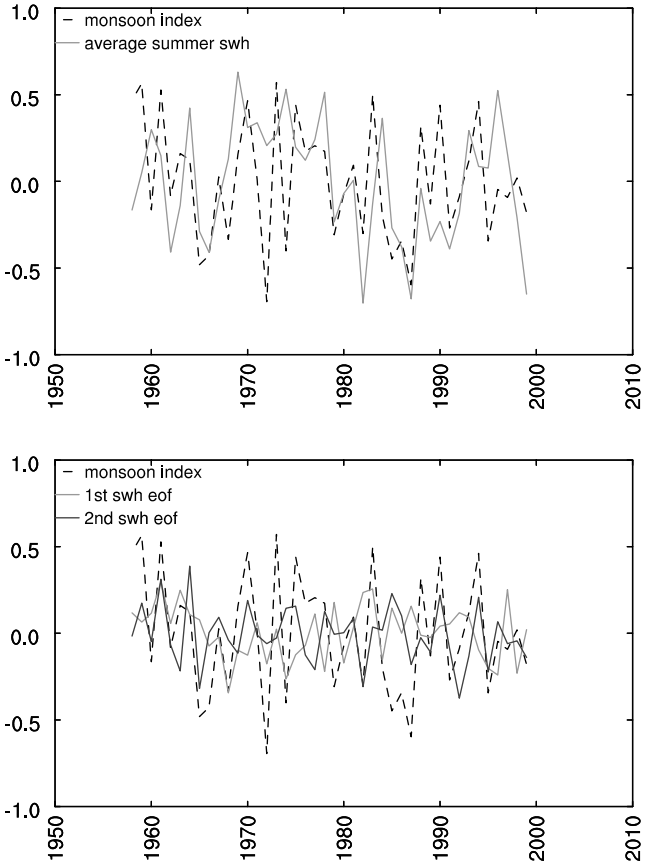

Fig. 16 Time series of Monsoon index and summer SWH plotted over a 42-year period (Monsoon data available only until 1999 and for summer). *Top panel* shows Monsoon index (*dashed black line*) and average summer SWH index (*light grey continuous line*). *Bottom panel* shows Monsoon index (*dashed black line*), average summer values of first PC (*light gray continuous line*) and second PC (*dark gray continuous line*)

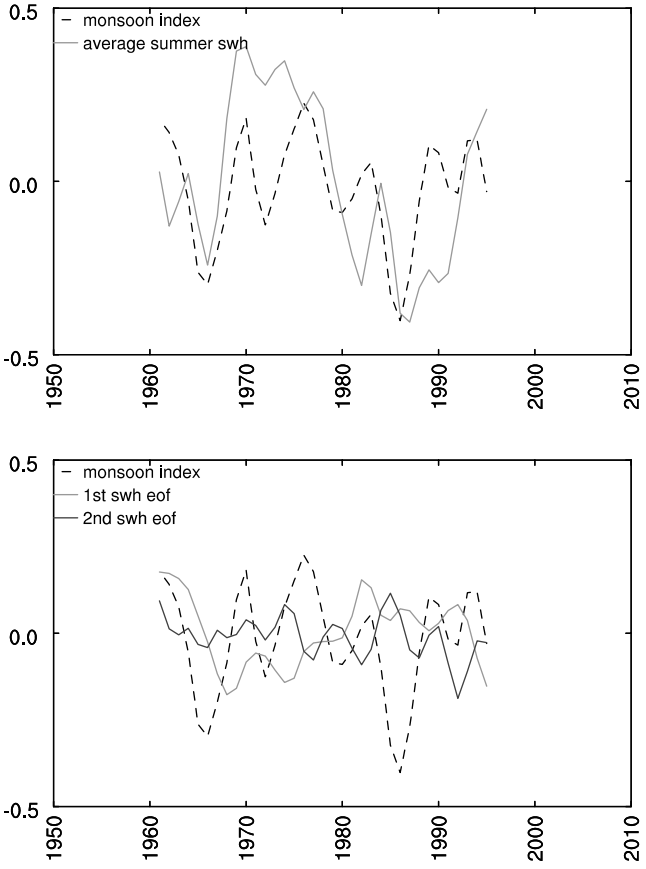

Fig. 17 Same as previous Fig. 16 but 5-year low-pass filter is applied to the data. The period 1962–1996 is plotted

(Gulf of Biscay) which moves to the Algerian basin in the summer-2 pattern. These characteristics reflect once more the importance of combination of wind regimes and fetch in determining wave climatology.

5 Conclusions

The SWHERA40 simulation, though underestimating the SWH, can be used for reproducing the inter-annual variability of the monthly average SWH field. This conclusion is supported by its comparison with the SWHT213 simulation (forced by higher resolution wind fields), buoy and satellite observations. All these set of data are available during the last decade of the twentieth century, and are too short for evaluating multi-decadal trends and climate variability, which can instead be investigated by the SWHERA40 with its 44-year duration.

The first part of this study has analysed the characteristics of inter-monthly variability and the mean annual cycle. The PCA of the monthly averaged wave fields has produced two principal wave regimes, which together explain most SWH variability (73%). The first EOF shows a pattern whose positive phase is dominated by the action of Mistral. This regime determines a wave field which propagates southeastward in the western part and turns eastward over the rest of the Mediterranean, following its shape until the eastern coast. The negative phase is dominated by the presence of high southward propagating waves in the Aegean Sea and Levantine Basin associated to the action of the Etesian winds. The second EOF exhibits a pattern due to the effect of both Libeccio (in the Tyrrenian sea) and Sirocco (in the Ionian sea), which determine northeastward and northward propagating waves, respectively. Consequently, the first and the second EOF are called Mistral-Etesian and Libeccio-Sirocco SWH patterns, respectively. The Mistral-Etesian pattern is associated to a SLP field with a low pressure centred above northern Italy and the Alps, whose anti-clockwise circulation covers the whole Mediterranean Basin (positive phase), and to its reversal to a high pressure above continental

Fig. 18 Same as Fig. 14, but showing summer SLP composites and using the Indian Monsoon index deviations from its mean summer cycle

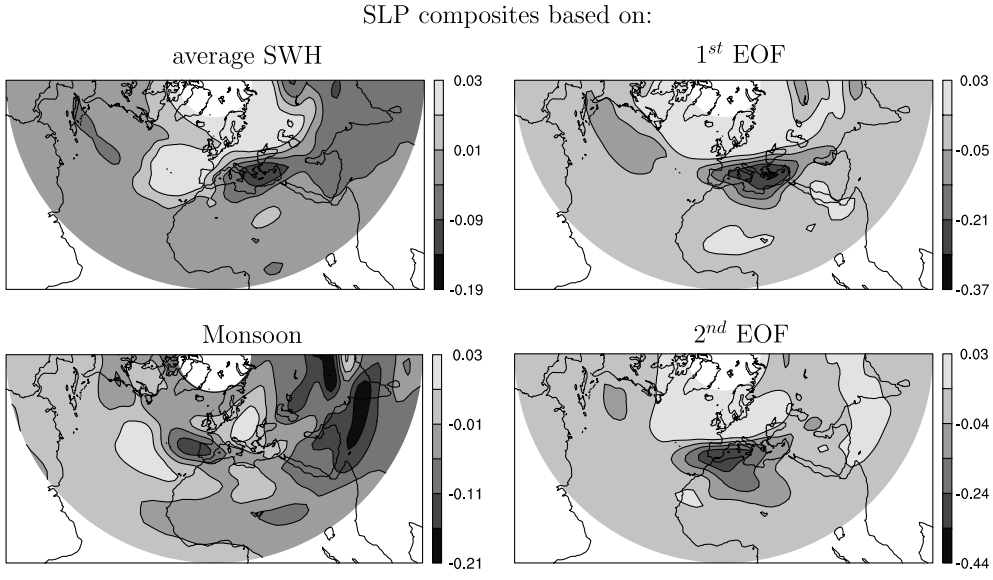

Europe with intense clockwise circulation in the eastern Mediterranean (negative phase). The Libeccio-Sirocco pattern is associated with a low pressure above the Gulf of Genoa in the NorthWest Mediterranean Sea, with northward circulation in the central part of the Mediterranean Sea (positive phase) switching to a south-westward SLP gradient (negative phase). Inter-monthly variability of the first and second PCs allows the identification of seasonality of the SWH field. Two main seasons are recognizable: winter (Dec-Jan-Feb-Mar) and summer (Jun-Jul-Aug-Sep), characterised by the positive and negative phase of Mistral-Etesian-pattern, respectively. Fall (Oct-Nov) and spring (Apr-May) are, instead, characterised by a positive phase of the Libeccio-Sirocco-pattern. As the first EOF is concerned, fall and spring appear seasons characterised by its transition to the positive and the negative phase, respectively, but with large inter-annual variability.

Patterns of inter-annual variability were analysed, relative to the above mentioned seasonality. The linear regression, performed upon the time series of monthly averaged SWH field for the 44-year period examined, reveals a statistically significant tendency to a reduction of SWH in the winter season. Winter average SWH results anti-correlated with the NAO index so that SWH decrease consistently corresponds to the increase of the NAO index. The SWH trend corresponds to a similar trend of both the first and the second PCs, both correlated with NAO. In summer, a much weaker statistically significant correlation exists between the second EOF pattern and the Indian Monsoon index. However, the SLP composites based on large positive/negative SWH values do not permit to re-construct the large scale SLP patterns associated to NAO and Indian Monsoon. The SLP composites are dominated by centres of action located above or near Mediterranean Sea, which appear responsible for regional atmospheric circulation features which are associated with wave regimes more closely than the relatively remote features of large scale patterns (NAO, Monsoon). Essentially, SLP patterns associated to the inter-annual variability of seasonal wave regimes are characterised by a single deep minimum located above central Europe (winter-1 pattern), Aegean Sea (summer-1 pattern), Gulf of Biscay (winter-2 pattern), Algerian Basin (summer-2 pattern)

This analysis stresses that wave dynamics in Mediterranean is strongly influenced by the regional orographic conformation and fetch. Though large scale patterns (mainly NAO) influences the average SWH field, their effect is strongly modulated by mesoscale factors and geographical land-sea distribution. In fact, the influence of NAO is distributed between the first and second EOFs, so that its characteristic dipole is not recognizable as dominant in the SLP patterns associated to the SWH variability. In conclusion, the role of fetch and the orientation of Mediterranean Basin with respect to the atmospheric circulation appears fundamental in the SWH variability regimes. The fetch acts as a filter, selecting surface atmospheric circulation components where regional characteristics conform to the shape of the basin and, therefore, are more effective in producing waves. This modulation implies that wave variability regimes reflect regional features, directly responsible for the wave generation, more than large scale patterns, though a link to NAO and Indian Monsoon is certainly present.

Acknowledgements The RON observations dataset has been provided by the APAT agency (Agenzia per la Protezione dell'Ambiente e servizi Tecnici, environmental protection agency and technical services). Data are available at http://www.telemisura.it. Figure 11 and results of linear regression analysis, shown in Table 3, were obtained using the Graphpad Prism software, version 4.00 for Windows, San Diego, California USA, demo available at http://www.graphpad.com. Time series of Indian Monsoon observed data have been downloaded from the Indian Institute of tropical Meteorology web site, http://www.tropmet.res.in.

References

Buzzi A, Tibaldi S (1978) Cyclogenesis on the lee of Alps: a case study. Quart J Roy Meteorol Soc 104:171–287

Cavaleri L, Bertotti L (2004) Accuracy of modelled wind and waves fields in enclosed seas. Tellus 56(2):167

Cavaleri L, Bertotti L, Lionello P (1991) Wind-wave cast in the Mediterranean sea. J Geophys Res 96C:10739–10764

Günter H, Rosenthal W, Stawarz M, Carretero JC, Gomez M, Lozano I, Serano O, Reistad M (1998) The wave climate of the Northeast Atlantic over the period 1955–94: the WASA wave hindcast. Global Atmos Ocean System 6:121–163

Hoskins BJ, Hodges KI (2002) New perspectives on the Northern Hemisphere winter storm track. J Atmos Sci 59:1041–1061

Hurrell JW (1995) Decadal trends in the North Atlantic Oscillation: regional temperatures and precipitation. Science 269:676–679

Jones PD, Jonsson T, Wheeler D (1997) Extension to the North Atlantic Oscillation using early instrumental pressure observations from Gibraltar and South-West Iceland. Int J Climatol 17:1433–1450

Kripalani RH, Kulkarni A (2001) Monsoon rainfall variations and teleconnections over south and east Asia. Int J Climatol 21:603–616

Lionello P, Elvini E, Nizzero A (2003) Ocean waves and storm surges in the Adriatic Sea: inter-comparison between the present and doubled CO_2 climate scenarios. Clim Res 23:217–231

Simmons AJ (1991) Development of the operational 31-level T213 version of the ECMWF forecast model. ECMWF Newslett 56:3–13

Simmons AJ, Gibson JK (2000) The ERA-40 project plan, ERA-40 project report series n.1

Trigo IF, Bigg GR, Davies TD (2002) Climatology of cyclogenesis mechanisms in the Mediterranean. Mon Wea Rev 130:549–649

Von Storch H, Zwiers FW (1999) Statistical analysis in climate research. Cambridge University Press, Cambridge

WAMDI group, Hasselmann S, Hasselmann K, Bauer E, Janssen PAEM, Komen G, Bertotti L, Lionello P, Guillaume A, Cardone VC, Greenwood JA, Reistad M, Zambresky L, Ewing JA (1988) The WAM model—a third generation ocean wave prediction model. J Phys Oceanogr 18:1776–1810